Journal of Alloys and Compounds 884 (2021) 161056

Contents lists available at ScienceDirect

Journal of Alloys and Compounds

journal homepage: www.elsevier.com/locate/jalcom

Growth and characterization of ZnO thin films at low temperatures: from room temperature to − 120 °C

Carlos Morales[a,b], Dietmar Leinen[c], Adolfo del Campo[d], José Ramón Ares[e], Carlos Sánchez[e], Jan Ingo Flege[b], Alejandro Gutiérrez[a], Pilar Prieto[a], Leonardo Soriano[a,*,1]

[a] Departamento de Física Aplicada and Instituto de Ciencia de Materiales Nicolás Cabrera, Universidad Autónoma de Madrid, Francisco Tomás y Valiente 7, E-28049 Madrid, Spain
[b] Applied Physics and Semiconductor Spectroscopy, Brandenburg University of Technology Cottbus–Senftenberg, Konrad-Zuse-Strasse 1, D-03046 Cottbus, Germany
[c] Departamento de Física Aplicada, Universidad de Málaga, Campus Teatinos, E-29071 Málaga, Spain
[d] Instituto de Cerámica y Vidrio, ICV-CSIC, Kelsen 5, E-28049 Madrid, Spain
[e] Departamento de Física de Materiales and Instituto de Ciencia de Materiales Nicolás Cabrera, Universidad Autónoma de Madrid, Francisco Tomás y Valiente 7, E-28049 Madrid, Spain

ARTICLE INFO

Article history:
Received 24 March 2021
Received in revised form 24 June 2021
Accepted 2 July 2021
Available online 6 July 2021

Keywords:
ZnO
Thin films
Morphology
SEM
DRX
Optical properties
Electrical properties

ABSTRACT

ZnO thin films have been grown by e-beam evaporation in the range from room temperature to − 120 °C on two types of substrates, Al_2O_3 (0001) and Si (100). Although the ZnO/Al_2O_3 system has been thoroughly characterized, including optical and electrical techniques, the morphological, structural and chemical properties show no significant differences between both substrates. Thus, the general features of the ZnO growth mode at low temperature can be generalized. The relatively low growth temperatures reduce the diffusion of atoms at the surface, which leads to morphological and chemical changes. As the temperature decreases, the growth mode changes from a van der Drift model to a gradual bilayer system composed of an interfacial layer in contact with the substrate and a second columnar-based layer. This second well-ordered film disappears for the lowest temperatures while a Zn-rich interface in contact with the substrate emerges. Precisely from this interface, Zn-rich whiskers develop under the ZnO film and cause the loss of adhesion at temperatures below − 100 °C. These extreme temperatures also affect the crystal size, lattice strain, and total amount of oxygen vacancies. The behavior of the optical and electrical properties in terms of band gap, transparency, electrical resistivity, and Seebeck coefficient is discussed in the light of structural and chemical characterization. Samples grown at 0 °C exhibit an enhanced transmittance compared to those grown at room temperature while preserving similar electrical resistivity values and natural n-type doping. These results open a promising route to enhance ZnO films properties below the typical high temperature window.

1. Introduction

ZnO is an intensely studied semiconductor characterized by its wide band gap at room temperature (RT) (Eg ~ 3.3 eV) and large exciton binding energy (~60 meV) [1–3]. Besides, high levels of charge carriers can be introduced into ZnO by heavy substitutional doping (n-type) while preserving good transparency. These properties have boosted ZnO as a low-cost candidate to substitute indium tin oxide (ITO) as a transparent conducting oxide in many applications [4,5]. ZnO thin films also find many other uses in a wide range of fields such as optoelectronics [6,7], gas sensors [8] or solar cells [9]. Nevertheless, limitations on achieving p-type doped ZnO films have moved the scientific focus to ZnO nanostructures, enhancing and tuning the oxide properties [10].

High-quality ZnO thin films and nanostructures can be grown by multiple physical and chemical deposition techniques. Regarding the first type, we can mention sputtering [11], molecular beam epitaxy (MBE) [12] or electron beam evaporation [13], whereas among the chemical methods, atomic layer deposition (ALD) [14], sol-gel [15], or metalorganic chemical vapor deposition (MOCVD) [16] stand out.

---

[*] Corresponding author.
E-mail address: l.soriano@uam.es (L. Soriano).
[1] ORCID: 0000-0001-5715-376X

https://doi.org/10.1016/j.jallcom.2021.161056
0925-8388/

Despite their differences, the main parameter for all these growth techniques is the temperature, which significantly influences the final ZnO properties. In this regard, multiple comparative studies on ZnO nanostructured films have dealt with their physical properties and growth morphology as a function of this parameter. For example, the work of J. Y. Park et al. [17] shows significant morphological differences in ZnO films deposited by MOCVD in the range 100–500 °C, whereas Cho et al. [18] studied how ZnO thin films grown by sputtering present variations of the optical and electrical properties as a function of the growth temperature (100–400 °C). In general, adequate crystallinity, transparency and electrical conductivity levels require temperatures above 500 °C, although for industrial processes these temperatures translate into high costs and possible degradation of device materials by diffusion between components. Post-annealing treatments face similar problems. These issues are why in the last years considerable efforts have been devoted to decrease the growth temperature while preserving good chemical and physical properties of ZnO. Although some competitive results have been obtained for growths performed at room temperature (RT) [19,20], the general compromise between low-temperature and high-quality films is established in the range from 200° to 400°C.

The possibility of reducing the growth temperature below RT can imply changes in the growth mode by decreasing, or even totally suppressing, active thermal diffusion mechanisms at the surface [21]. These changes could affect the structural and chemical properties of the ZnO films, such as size and crystallographic orientation of crystallites, lattice strain, or density of typical ZnO defects such as oxygen vacancies and interstitial zinc incorporation. Eventually, this would affect the optical and electrical properties too. Chemical deposition techniques should be avoided in very low temperature ranges due to the low kinetics or total suppression of the chemical reactions.

The present work focuses on how low temperatures (RT to −120 °C) affect the growth mode, structure and composition of ZnO thin films deposited by electron beam evaporation. Although the complete characterization, including optical and electrical properties, has been carried out for the ZnO/Al_2O_3 system, films grown on Si substrates show very similar morphological, structural and chemical features. The comparison of both substrates allows a broader picture of the growth of ZnO at these low temperatures and the generalization of the main ZnO growth mode characteristics. Such low temperatures play a very important role in the ZnO early stages of growth, especially at the ZnO/substrate interface, giving rise to the formation of Zn-rich whiskers at the lowest temperatures, ultimately causing the loss of film adhesion. Optical and electrical measurements will be discussed in the light of previous morphological, structural and chemical characterization. The obtained columnar-based films present promising optical and electrical properties and may find multiple applications without compromising other device parts during the deposition process.

2. Experimental details

ZnO thin films have been grown by electron beam evaporation (EV1–8 from Ferrotec) using ZnO powder (99,99%, Goodfellow) as evaporation material using a molybdenum crucible. The base pressure of the growth chamber was below 10^{-7} mbar. Before each evaporation, the target was degassed for several minutes until the total pressure was below 10^{-5} mbar. The growth rate was tracked and controlled by a quartz crystal microbalance, set to approximately 30 nm/min. The evaporator emission current and voltage were set at 10 mA and 4.8 kV, whereas the distance between target and sample was around 50 cm. The sample holder was especially fabricated to accomplish substrate temperatures between − 195 °C and 200 °C. Fig. SI 1 of the Supporting Information shows a schematic of its design. Samples were grabbed by Ta clamps to a 3 mm thick Cu sheet situated above the stainless steel reservoir for liquid nitrogen (LN2) connected to the outside. This Cu sheet allows an uniform temperature distribution. Besides, the sheet is perforated to enable the pass of a heating cable (W, ø 0.25 mm), which is insulated from the Cu by ceramic tubes. For higher temperatures, an electrical current is supplied to the heating cable. The sample holder is located above the LN2 reservoir and the Cu block, continuously cooled during the growth by a constant flux of LN2. In the absence of extra-heating, it reduces the temperature down to − 195 °C. The temperature is monitored by a k-type thermocouple.

Two types of substrates were used to study the possible influence on the growth morphology and allow the optical and electrical characterization through different techniques depending on the substrates nature. In this sense, single-crystalline wafers of Al_2O_3 (0001) (99.99%, Siegert Wafers) and Si with (100) orientation (p-type, CZ growth type, Siegert Wafers) were used as flat substrates. All substrates were ultrasonically cleaned by immersing them subsequently into acetone and methanol. As a final cleaning step, the samples were heated in vacuum up to 150 °C for 30 min before the evaporation process. For each growth temperature both, Al_2O_3 and Si substrates were placed simultaneously into the sample holder.

The morphology of the deposited ZnO films was studied by high-resolution scanning electron microscopy (SEM), using a field emission gun-scanning electron microscope (Philips XL30 S-FEG) at an accelerating voltage of 20 kV. Besides, high-resolution SEM and EDX images and mappings, respectively, were taken with a Dual Beam Helios NanoLab 650 (FEI) microscope equipped with an electron field emission source (ElstarTM XHR) and a beam energy in the range between 20 and 30 keV. X-ray diffraction (XRD) measurements were carried out with a Panalytical Xpert PRO diffractometer equipped with a secondary graphite monochromator, using CuK_α monochromatic radiation in grazing-incidence condition. XRD data were collected using a $\theta/2\theta$ geometry with a beam incidence angle of 0.5° and a 2θ scan range between 20° and 80° with a step size of 0.04° and a counting time of 4 s/step. The XRD data were used to calculate the lattice strain and the mean crystallite size using the Scherrer approximation. Ex-situ XPS measurements were performed with a CLAM-4 MDC hemispherical electron analyzer from Thermo Fisher Scientific, using Mg K_α and Al K_α radiation alternatively to avoid overlapping of the Auger structures and the analyzed photoemission peaks. The pass energy was set at 20 eV, giving an overall resolution for each anode of 0.9–1.0 eV, respectively. The energy scale was calibrated using the C 1 s peak of adventitious carbon at 284.8 eV [22]. Finally, ex-situ Raman spectra were taken with a confocal Raman microscope (Witec ALPHA 300RA) using a laser excitation at 532 nm and incident power of 1 mW, with an overall spectral resolution of 0.02 cm^{-1}. The Raman spectra show the average information of an XZ mapping with 3 µm of total depth. In addition, a pressed ZnO powder sample was used as reference for the XPS and Raman measurements.

The study was completed with optical and electrical measurements using thin films grown on insulating and partially transparent Al_2O_3 substrates. In particular, the ZnO band gap and grade of transparency was estimated from absorbance measurements using a CARY 100 Bio spectrophotometer without integration sphere. The optical density of the Al_2O_3 substrates taken as baseline is shown in Fig. SI 2. Regarding the electrical properties, two complementary techniques were used. First, the films electrical resistivity was measured from RT to T-NL2 (−195 °C) by the Van der Pauw method using a HMS-5000 system from Ecopia. Besides, thermoelectrical measurements of the Seebeck coefficient were performed with a homemade system [23]. This setup consists of a pair of aluminum blocks, with embedded heaters that act as thermal reservoirs and allow varying the average temperature and the thermal difference along the sample (ΔT). ΔT is measured by two thermocouples

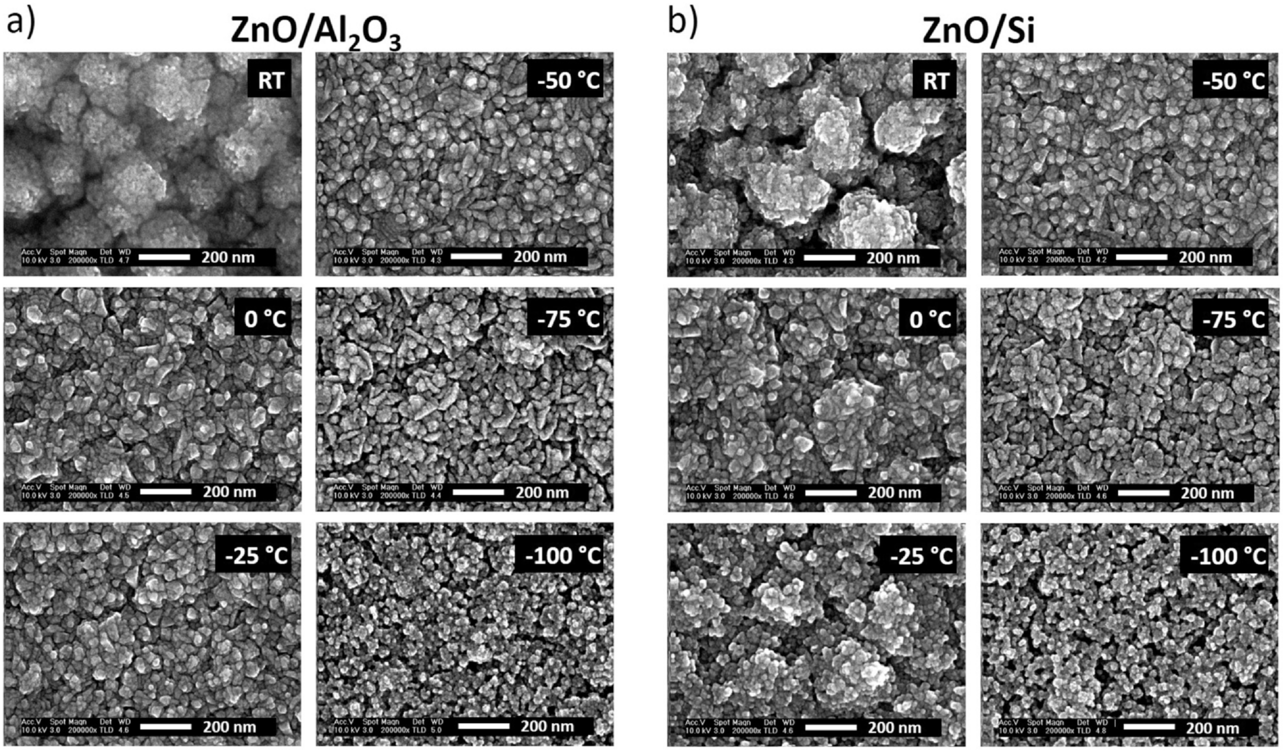

Fig. 1. High-resolution SEM images for a) ZnO films on Al_2O_3 and b) Si single crystals for different growth temperatures. The image at RT of ZnO/Al2O3 is blurred due to a charging effect induced by the insulating substrate.

attached to the film. The Seebeck voltage (ΔV) across the sample is monitored with two voltage probes, also attached to the films. Thermovoltage measurements were carried out reaching ΔT~5 °C.

3. Results and discussion

3.1. Structural and chemical characterization

Fig. 1 shows SEM top-view images of ZnO samples grown on Al_2O_3 (a) and Si (b) substrates at different temperatures (RT ZnO/Al_2O_3 sample is slightly blurred due to surface charging effect). Films deposited on both substrates show almost identical features. For the sample grown at RT, the ZnO film presents clusters composed of multiple grains with sharp edges, suggesting a polycrystalline growth with different crystallites showing up on the surface. As the growth temperature decreases (−50 °C), the clusters tend to merge, forming a more compact and uniform structure composed of grains with well-defined angles. For lower temperatures (−100 °C) the grain size decreases further while small pores and holes appear between them.

The left panel of Fig. 2(a, b and c) shows cross-sectional SEM images of three different ZnO deposits on Si substrate (RT, −50 °C and −100 °C, respectively), shedding light on the growth mode evolution. We want to remark that, due to the significant similarities between SEM top-view images on both substrates, the following description can be generalized and also hold on the Al_2O_3 substrates. As can be seen in Fig. 2a the deposits at RT are characterized by the coalescence of individual clusters that grow mainly vertically and slightly towards the sides in a V shape. First, the nucleation density on the substrate seems to be low, dominating the vertical crystal growth over other directions, thus inducing the formation of clusters that grow slowly towards the sides until contact adjacent clusters. This process induces the formation of a non-compact deposit during the first tens of nanometers. Second, the length of ZnO grains gradually increases with the distance from the substrate, forming a pseudo-columnar structure in which each of the grains on the top view image refers to a specific vertical grain, composed by aligned crystallites grown on that preferential orientation. This growth mode fits well with the model proposed by van der Drift [24] (see Fig. 2d scheme). At temperatures close to RT, surface diffusion would dominate. The deposited atoms could move a limited number of "steps" stacking on facets with lower surface energy, promoting distinct crystallographic directions and inducing a columnar-based structure.

Moving towards lower temperatures, cross-sectional images for ZnO/Si films are in correlation to those of top view, whereas important differences are observed in comparison to the RT sample (cross-sectional images for ZnO/Al_2O_3 are almost identical but with worse quality, blurred, -not shown here-). As temperature decreases to − 50 °C, two different layers can be appreciated (Fig. 2b). The first layer in contact with the Si substrate shows a morphology with more softened and smoother edges, resembling a considerable reduction of the crystal size. A second columnar-based layer grows on top of the first one, more compact than in the RT case. A similar bilayered behavior composed of a less ordered interfacial layer followed by a second well-structured ZnO layer (usually columnar) has been previously reported in the literature for both Si (100) and Al_2O_3 (0001) substrates using MOCVD at higher temperatures [17,25,26]. Nevertheless, the height of the present interfacial layer is larger than in previous works [17,25,26], probably due to the lower diffusion rates on the surface at lower temperatures, thus delaying the growth of a preferential orientation. Indeed, at − 100 °C the first layer seems to grow in the same way while the columnar-based layer disappears (Fig. 2c). It is worthy to note some particularities. First, the smooth image indicates that the reduction of the crystallite size continues, forming a compact layer that somehow recalls a vertical growth. However, a non-compact area characterized by a fibrous-like structure with hollow areas appears at the ZnO/Si interface. As we will discuss in more detail, this is the first step for the loss of adhesion. Once again, this reduction of the crystallites size and loss of the pure

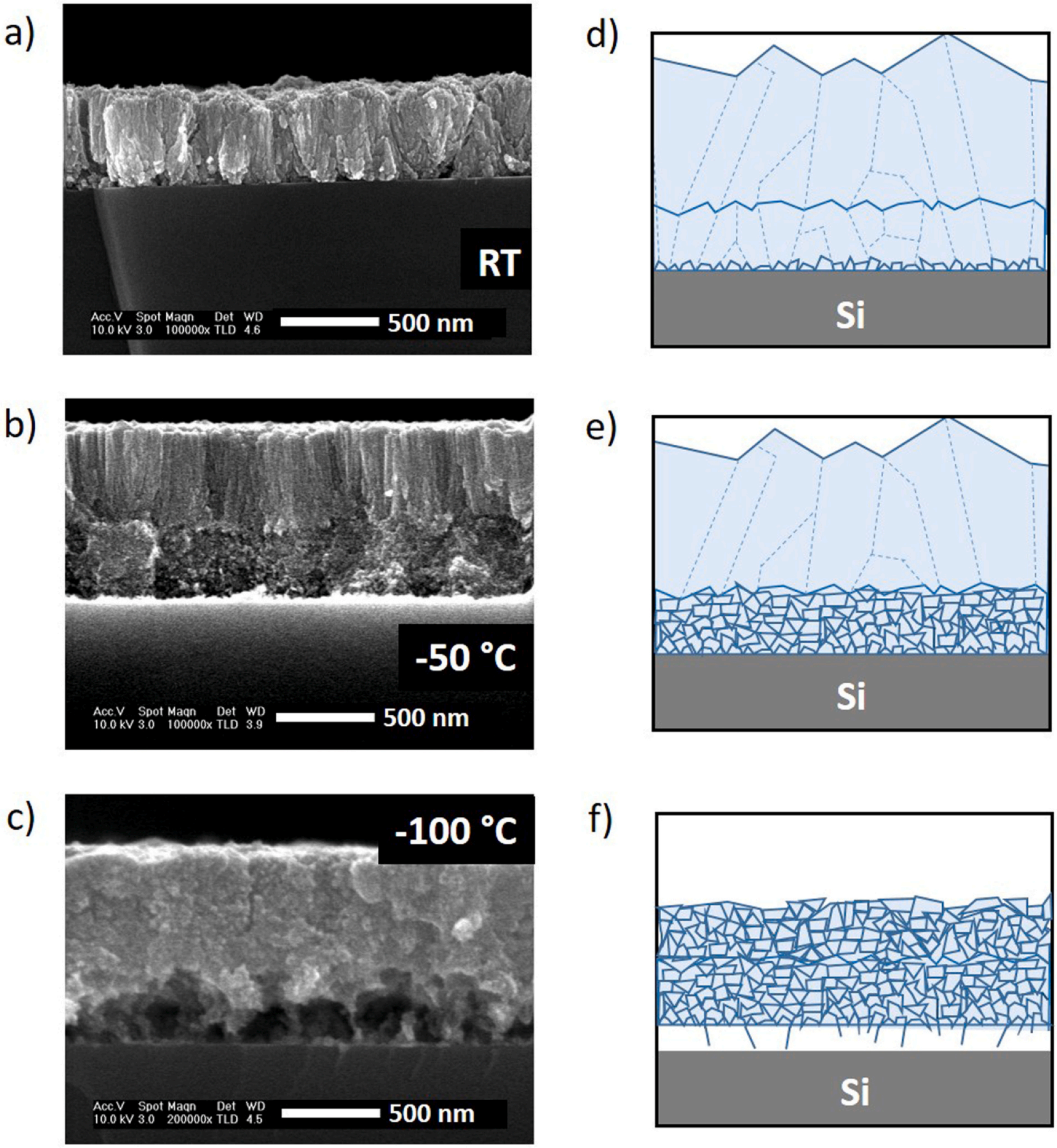

Fig. 2. High-resolution SEM cross-sectional images taken on the Si substrates for a) RT, b) − 50 and c) − 100 °C, respectively,. In the right panel, figures d-f show a schematic representation of the ZnO growth at RT, − 50 and − 100 °C, respectively.

columnar behavior could be related to a decrease of the surface mobility during growth. This low mobility reduces the possibilities to enhance the growth of preferred crystallographic orientations, inhibiting the well defined column growth.

Continuing with the morphological features of the grown ZnO films, Fig. 3 shows SEM images after deposition on Si at − 120 °C (a, b and c) and on Al_2O_3 (d) at − 100°C. The ZnO film grown on Si is mostly separated from the substrate; only some parts near the Ta clamps remain adhered. Nevertheless, interesting features can be observed in these images. Fig. 3a shows the ZnO unstuck backside layer, which shows a fibrous-like structure as that shown in Fig. 2c. However, the most surprising feature is the extremely long whiskers (> 15 µm) appearing under the thin film. The inset shows an image taken at higher magnification zoom at the junction point between this nanostructure and the backside of the ZnO film, demonstrating that the whisker grows from the ZnO film. The formation of such structures at the ZnO/Si interface is found all over the back side of the sample (Fig. 3b). In this case, the SEM picture has been taken on the top of a broken ZnO film. As can be seen, multiple whiskers appear between both sides of the fracture and along the perpendicular direction with respect to the film crack. These images suggest that the origin of the loss of adhesion would start with the formation of a fibrous-like layer (Fig. 2c, −100 °C) and the subsequent evolution of nanostructures that could finally detach the ZnO film. To clarify

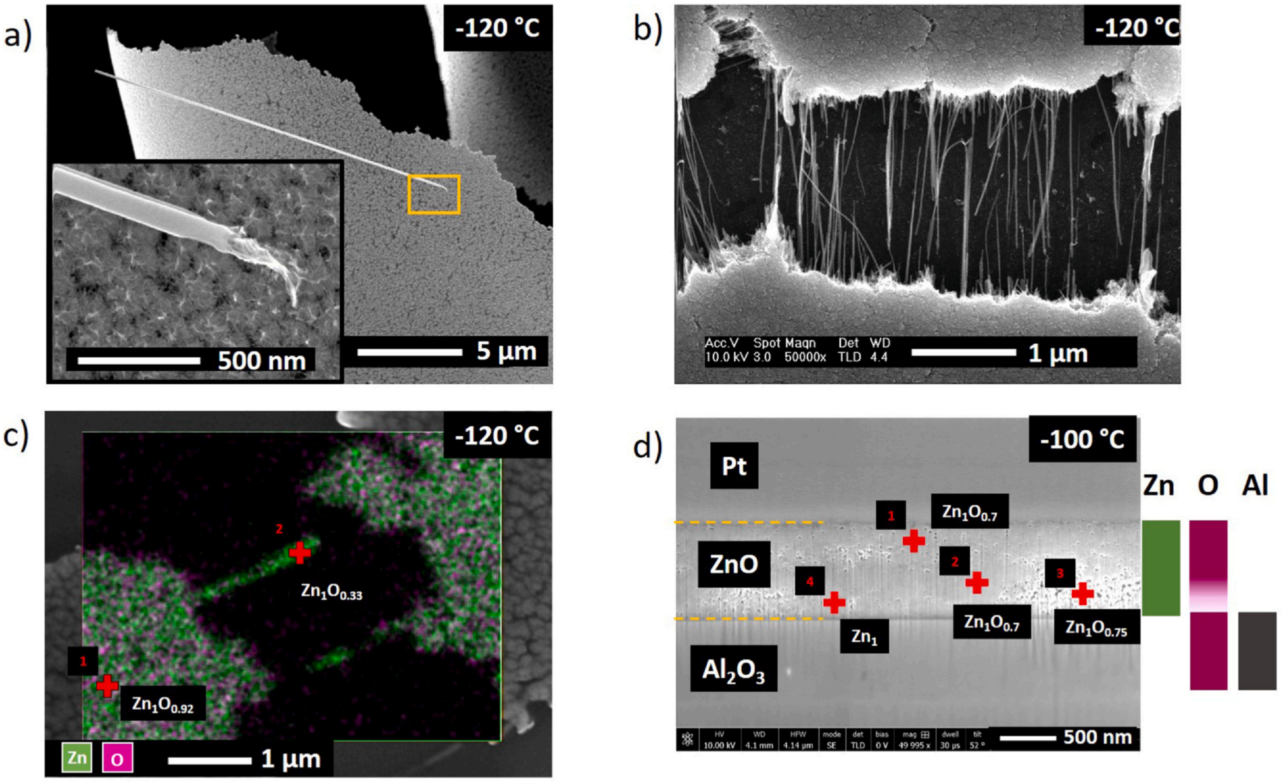

Fig. 3. SEM images of ZnO films grown at − 120 °C on Si (100) wafer: a) backside of the ZnO film; b) front side. Insert in a) shows a zoom of the yellow rectangle. c) EDX mapping of ZnO/Si sample grown at − 120 °C. Two local EDX spectra were taken inside the ZnO film (point 1) and at the nanostructure (point 2). The corresponding ZnO_x composition is indicated. d) Cross-sectional image performed by cutting with a focused ion beam a ZnO/Al_2O_3 sample grown at − 100 °C. Spatially resolved EDX local spectra were taken at different positions, and ZnO_x composition is indicated.

the nature of these nanostructures and the changes on the ZnO film, Fig. 3c shows an EDX mapping of the whiskers grown at − 120 °C on Si. Spatially resolved spectra taken on both, the film and the filament, show a Zn enrichment of these nanostructures, with almost 75% of Zn whereas the Zn/O ratio is almost 1:1 in the film (Fig. SI 3a presents the original spatially resolved EDX spectra).

Fig. 3d shows a series of local spectra along the cross-section of a ZnO/Al_2O_3 sample grown at − 100 °C. The transverse cut made with the ion beam has changed the morphology from what has previously been reported in Figs. 2 and 3a and b, although similar features can be observed, for instance, more porous areas near the substrate. Besides, EDX spectra taken at the ZnO/Al_2O_3 interface show a Zn enrichment, confirming the Zn-rich nature of this ZnO/substrate interface at such low temperatures (Fig. SI 3b shows the raw EDX spectra). The labels in Fig. 3d highlight the atomic Zn/O ratio at each position. Deviations from the expected Zn/O ratio 1:1 far from the interface are probably related to the alumina substrate signal. Although an enhanced oxygen background from the underlying alumina has been considered in the quantitative analysis, this form of background subtraction most likely remained incomplete, and the atomic concentrations should only be interpreted qualitatively to identify trends in composition.

The results from our structural and chemical characterization notwithstanding the origin of such Zn whiskers remains unclear. Recalling the previous discussion of the growth mode as a function of temperature, it seems surprising the formation of these well-ordered structures at the lowest temperatures (−120 °C). The formation of an initial Zn-rich layer at the interface could be related to the chemical interaction of the ZnO overlayer with the substrate. Once the e-beam sublimates the target, Zn-O species could decompose into Zn and O before reaching the surface. At relatively high temperatures, these atoms would be able to react and form ZnO on the surface, but decreasing the substrate temperature could prevent the oxide formation on the Si and Al_2O_3 surfaces. In fact, metallic Zn would be expected to agglomerate at the surface, leading to the formation of nanoclusters. Besides, silica and alumina are widely used as catalyst supports, and mainly referring to alumina, its higher Lewis acidity may facilitate the reduction of oxide compounds at its surface [27]. In this sense, at lower temperatures metallic Zn could nucleate first and serve as the seed for later ZnO growth. Simultaneously, this initial Zn deposit could facilitate the diffusion of the metallic atoms, inducing the fast growth of such long nanostructures along preferential orientations and causing the loss of adhesion.

To shed more light onto the structural details, a series of samples grown on both substrates have been characterized by XRD. Fig. 4a and b show the diffractograms for the ZnO films grown on Al_2O_3 and Si wafers at different temperatures, respectively. No significant differences were observed between samples grown on the different substrates. The principal crystallographic orientations for ZnO (hexagonal wurtzite structure, P63mc space group and lattice parameters a = 3.2498 Å, b = 3.2498 Å, and c = 5.2066 Å) and metallic Zn are plotted at the bottom for comparison (reference data from JCPDS-ICDD 00–036–1451 and JCPDS-ICDD 00–004–0831 for ZnO and Zn, respectively). However, no contribution from the metallic phase is observed. This discrepancy with cross-sectional EDX data could be explained by the grazing nature of the XRD measurements (incidence angle of 0.5°, see Experimental section for more details). Under this configuration, the total depth that X-ray could penetrate is around 0.6 µm (considering three times the attenuation depth for ZnO in this configuration [28]). Thus, considering the thickness of the films (~800 nm), the ZnO/substrate interface could not be measured. With this in mind, the discussion will be focused on the (100) peak at ~32°, the (002) peak at ~34.6°, and the (101) peak at ~36.5°. Comparing to the ICDD card, the (002) has a relatively higher

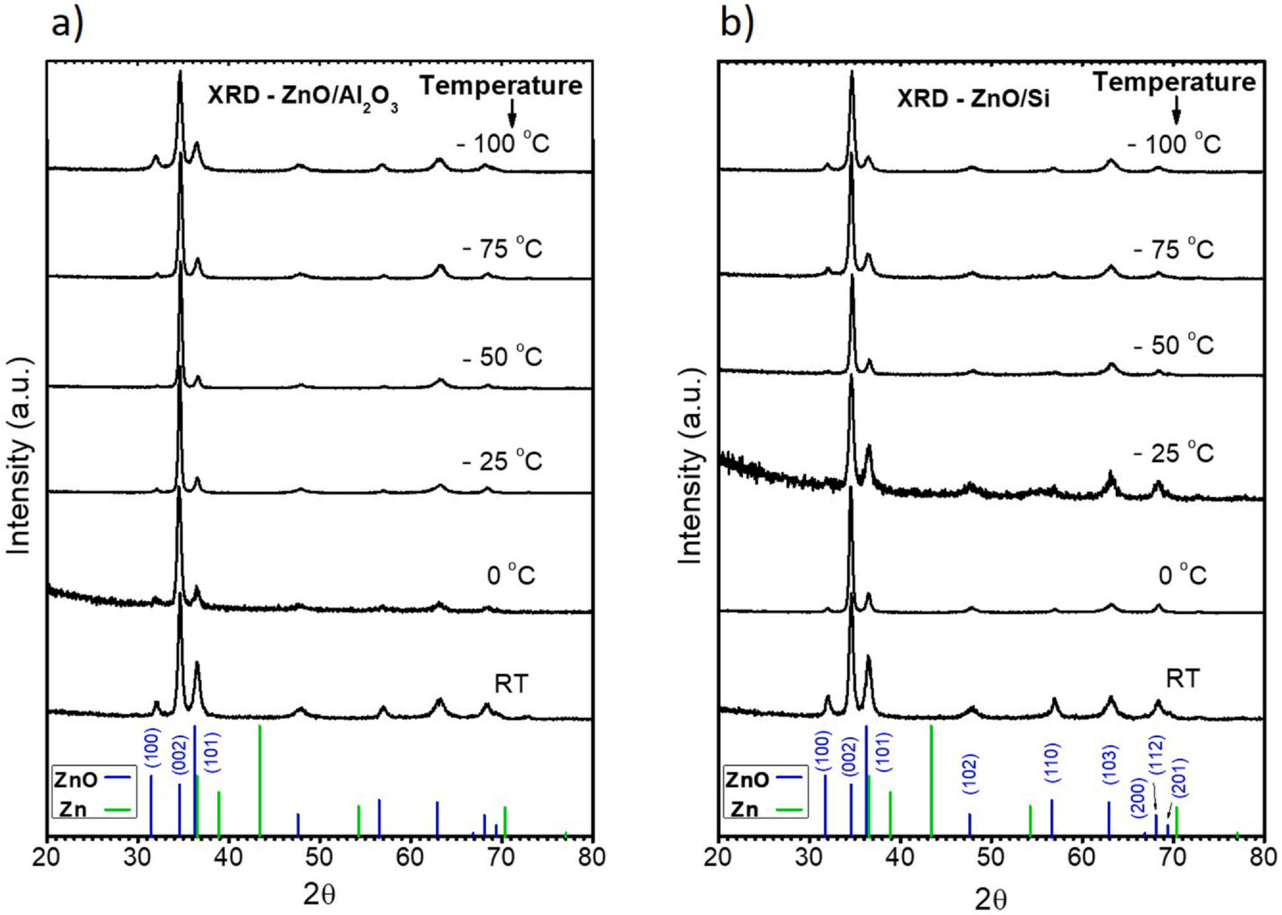

Fig. 4. X-ray diffraction patterns of ZnO films grown on a) Al_2O_3 (0001) and b) Si (100) single crystal wafers at different temperatures. Metal Zn (JCPDS 00–004–0831) and ZnO (JCPDS 00-036-1451) diffraction peaks are also indicated.

intensity for all temperatures. This circumstance confirms the preferential c-axis growth orientation, which is a well-known behavior of ZnO since its (0001) plane has the lowest surface energy [29]. Minor contributions from (100) and (101) can also be found at all temperatures, being their signal amplified at RT and − 100 °C, precisely when the columnar growth is less marked.

Moreover, Fig. 5 shows the crystallite size and net strains calculated from the XRD patterns for both substrates. Regarding Fig. 5a and b, the mean crystal size of ZnO/Al_2O_3 and Si/ZnO films, respectively, can be calculated by the Scherrer approximation with a confidence range of 10%. In all cases, the original data for (002) and (101) peaks were fitted using a pseudo-Voigt curve. As it can be seen, the size in both orientations increases from RT to − 50 °C, in correspondence with the morphological transition from clusters to a more compact columnar-based layer (see Figs. 1 and 2). Only the sample grown at − 25 °C on Si, whose diffractogram shows a worse signal-to-noise ratio, breaks this tendency. Besides, crystallites in the (002) direction are 50% larger than in the (101) direction at all growing temperatures, as it is expected for preferred orientation. From − 50 °C to − 100 °C, the crystal size gradually decreases, in line with the enlargement of the interfacial layer characterized by smaller grains and a loss of the preferred orientation character. The lattice parameters could also be calculated from the positions of the Bragg diffraction peaks. Fig. 5c and d show the strain in the *c*-axis (out-of-plane) and *a*-axis (in-plane) directions of ZnO/Al_2O_3 and ZnO/Si films, respectively, by comparing the calculated lattice parameter with those of the ICDD card taken as reference. These strains can be calculated by $\varepsilon = [\alpha - \alpha_o]/\alpha_o$, where ε is the strain, α is the lattice parameter (*c* or *a*) of the grown ZnO films, and α_o is the lattice parameter of the ICDD card (c_o or a_o, respectively). As it can be noticed, both axes follow a similar behavior, increasing the strain (compressing) from RT to − 50 °C and subsequently relaxing it for even lower temperatures, showing the *a*-axis a larger strain. By keeping in mind the total X-ray penetration depth in the experimental setup and the SEM images, it seems that the columnar growth accumulates more stress than the other less ordered deposits.

By comparing our results with those from interfacial layers obtained using high-temperature MOCVD, there exist important discrepancies although the large difference in the growth temperature makes absolute comparison difficult. They claim that the disordered interfacial layer in ZnO/Al_2O_3 (0001) is more compressive, especially in the in-plane direction, and ZnO lattice only relaxes once the top whiskers nucleate [26]. In our case, the formation of a compact columnar layer instead of ZnO nanostructures such as nanowires or nanoneedles could be related to the limitations on surface diffusion processes due to the low temperatures. Nonetheless, the improvement of films crystallinity for films grown at moderately low temperatures (especially for −50 °C film) compared to RT could be related to the formation of this compact-based layer above the interfacial layer. At even lower temperatures (below −50 °C), these diffusion restrictions imply that deposited atoms would get stacked at the local minimum energy sites and not to positions more energetically favorable, increasing the strain and density of defects in the ZnO matrix and reducing the mean crystal size to only a few tens of nanometers while keeping the (002) orientation. Moreover, the decrease in compressive stress at the lowest temperatures could be related to the formation of Zn-based whiskers. Although the

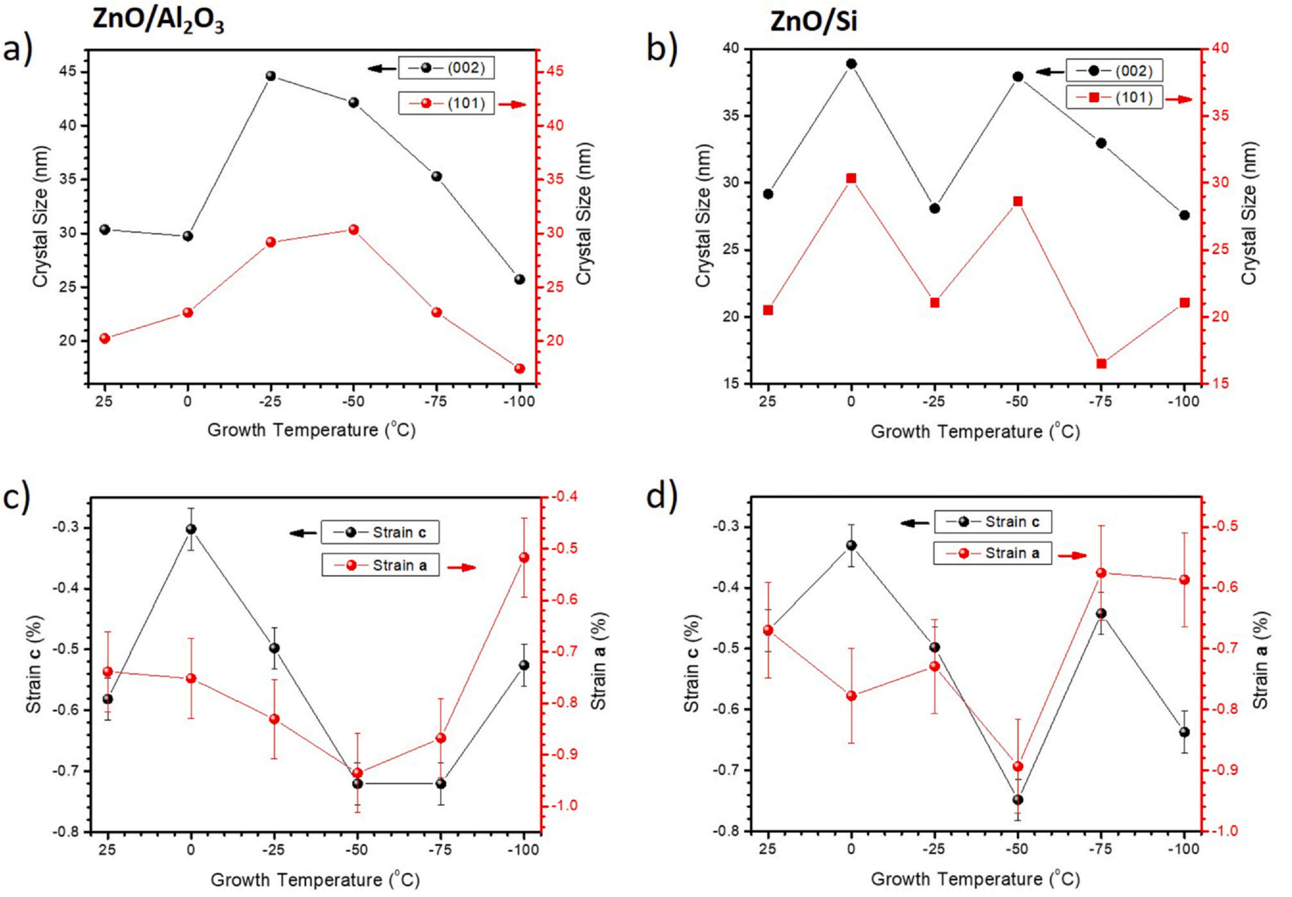

Fig. 5. Crystal size calculated from (002) and (101) diffraction peaks, black circles and red squares, respectively, for a) ZnO/Al_2O_3 and b) ZnO/Si films. The mean crystal size calculated by the Scherrer approximation has a confidence range of 10%. Strain of the c-axis and a-axis in relation to the JCPDS-ICDD 00–036–1451 card, black circles and red square, respectively, for c) ZnO/Al_2O_3 and d) ZnO/Si films.

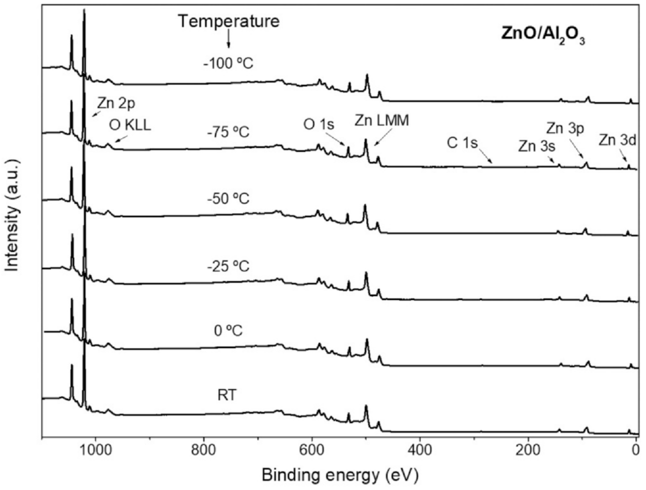

Fig. 6. XPS survey spectra for ZnO films grown on Al_2O_3 substrates at different temperatures.

formation mechanism of this type of metallic nanostructures is still under discussion, their growth seems to be favored by a relief of the accumulated stress [30,31]. Thus, a complex interaction between different factors (ZnO net stress, substrate reducing power and limitation of thermal surface diffusion with low temperatures) could determine different growths at the interface depending on the energy barriers fixed by those parameters.

Further XPS and Raman spectroscopy measurements were performed in order to study the presence of defects in the ZnO matrix. Fig. 6 shows the XPS survey spectra of films grown on Al_2O_3 substrates (see Fig. SI 4 for the equivalent ZnO/Si plot). In addition to Zn and O contributions, only small traces of adventitious carbon (C 1 s) from atmosphere exposure were observed. Fig. 7a shows the normalized Zn-LMM Auger spectra for all ZnO films grown on the alumina substrates (see Fig. SI 5a for ZnO/Si spectra). No differences between substrates were observed. The Auger Zn-LMM is very sensitive to the chemical environment of Zn atoms and is mostly used to study the composition and defects of ZnO deposits [32,33]. The measured spectra show the typical shape of ZnO (reference ZnO spectra is given, dotted line), and only a slight broadening at ~990 eV is observed, corresponding to the development of defects [33], in particular, oxygen vacancies. Raman measurements in Fig. 7b show the average spectra of the whole ZnO film, confirming at the ZnO bulk the same superficial results from XPS (see Fig. SI 5b for ZnO/Si Raman spectra). The ZnO spectrum is mainly characterized by the E_2^{low} band at ~99 cm^{-1} assigned to Zn sub-lattice, the E_2^{high} at ~439 cm^{-1} associated to oxygen vibrations and the defective band E_1(LO) at ~590 cm^{-1}, which is strongly affected by defects as oxygen vacancies [34]. The current Raman spectra present a broad band at 350–600 cm^{-1} with a maximum at the E_1(LO) contribution, indicating the existence of a significant number of oxygen vacancies, and thus supporting our previous conclusions based on XPS. During the XZ mapping, no spectral differences as a function of the thickness were observed, indicating that ZnO films present similar structural properties within the entire film. Besides, the absolute intensity decreases for the lowest growth temperature, directly related to the reduction of the total amount of ZnO as the films enrich

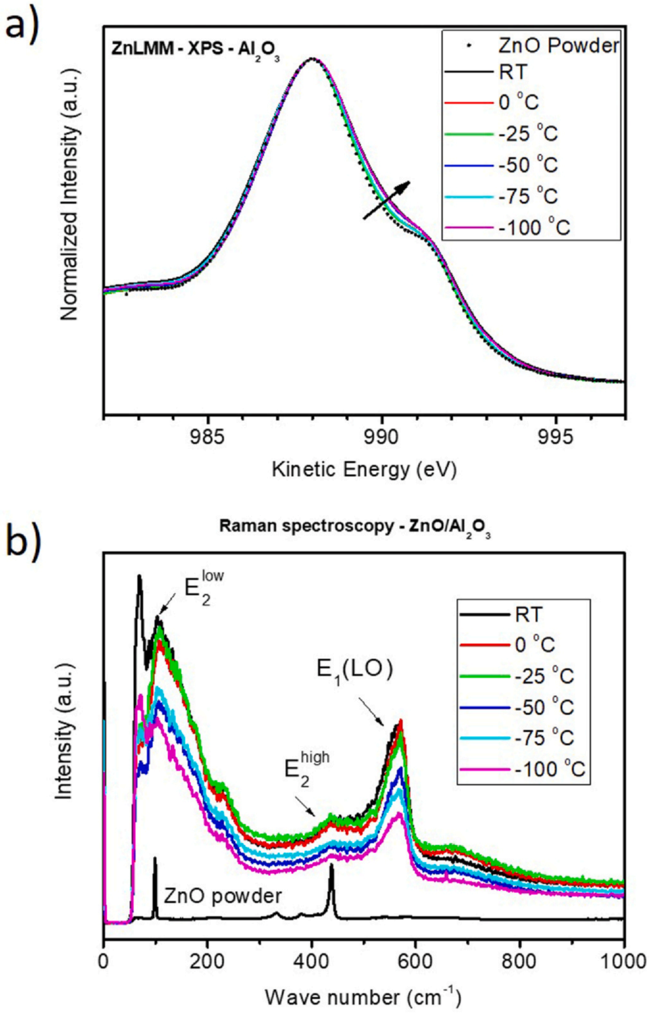

Fig. 7. a) Normalized Zn-LMM Auger spectra of ZnO films grown on Al_2O_3 (0001) single crystal. Dotted line: reference spectra from pure ZnO powder. b) Raman spectra of ZnO films grown on Al_2O_3 (0001) substrates. ZnO powder is shown as reference.

in Zn near the interface regions (as shown in Fig. 3). Our XRD, XPS and Raman analyses confirm a polycrystalline growth following the preferred (002) orientation, with a higher density of defects (mainly oxygen vacancies) at temperatures around − 50 °C, precisely for the films showing the best alignment and largest crystallite size of the columnar layer.

3.2. Optical and electrical properties

The optical and electrical properties of the ZnO films grown on transparent and insulating Al_2O_3 substrates have also been studied. Firstly, band gap values were estimated from the absorbance (A) spectra performed in the visible-UV range (1.5–4 eV). Fig. SI 6a shows the curves obtained by applying the formalism for allowed direct band gaps, $a^2 \propto h\nu$, where a is the absorption coefficient, and $h\nu$ is the photon energy. Except for the sample grown at − 75 °C where the optical absorption gap was not clearly defined, estimated values range from 3.18 to 3.29 ± 0.02 eV (see Fig. 8a, black circles). In addition to the allowed direct band gap equation, it could also be applied the Tauc ($A^2 \bullet (h\nu)^2 \propto h\nu$, [35]) and Pankove ($A^2 \propto h\nu$, [36]) formalisms for direct transitions on amorphous and polycrystalline materials, respectively. Their respective curves are plotted in Fig. SI 6 b and c. The obtained values are also represented in Fig. 8a being very similar to those using the first formalism. Although the band

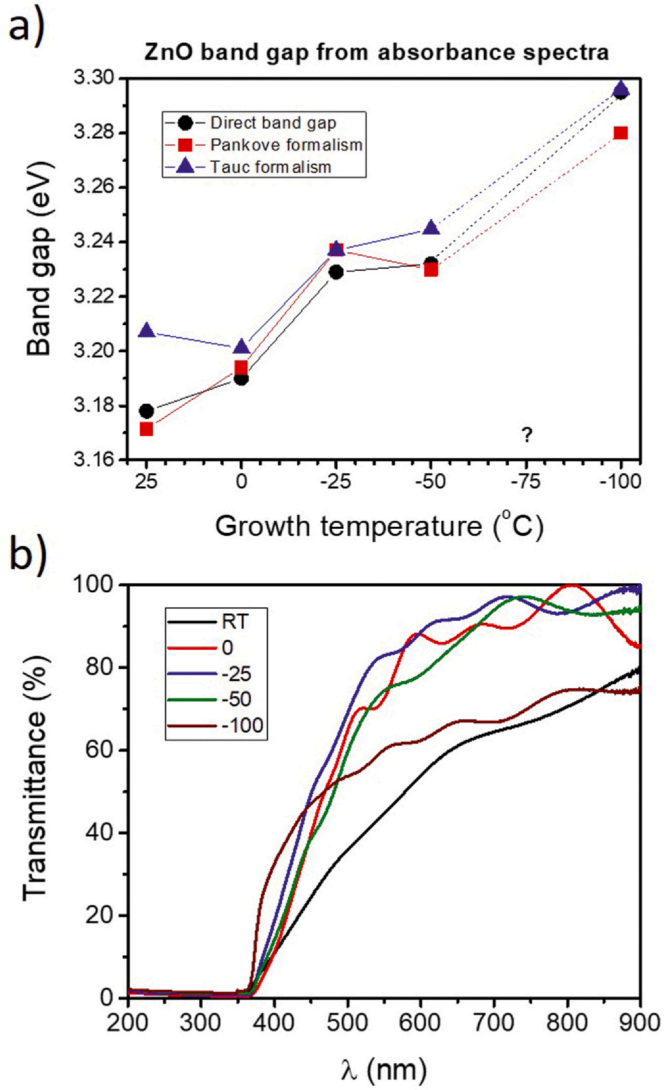

Fig. 8. a) Allowed direct band gap curves derived from absorbance spectra. Red dashed red line corresponds to 0 °C sample as an example of band gap estimation. b) Band gaps values as a function of growth temperatures. Value from sample grown at − 75 °C could not be estimated by this method.

gap slightly increases while the growth temperature decreases, these values are in the range of those expected for ZnO (Eg ~ 3.3 eV) and close to those reported in the literature for RT depositions [19,37–40]. Besides, Fig. 8b shows the transmittance of the films as a function of the wavelength. Those films grown between 0 and − 50 °C show transmittance values above 80%, corresponding to samples characterized by a columnar-based growth, with better crystallographic texture and larger crystallites. For most of them, the transmittance is significantly enhanced compared to RT and − 100 °C films, for which transmittance is limited to about a 60% and where the growth is more disordered, and thus, characterized by a larger density of grain boundaries. Nevertheless, it should also be noted that transmittance measurements were performed without an integration sphere (see experimental details), which could significantly affect rough samples, and thus explaining the RT film low transmittance (60%) compared to the literature values (> 80%) for the same deposition methods. As a note, the film grown at − 75 °C presents a very low transmittance (~20%) without a clear justification (surface or bulk contamination are discarded from XPS and EDX results), and thus has not been included in Fig. 8b (see absorption coefficient values in Fig. SI 6a). Transmittance is a complex property

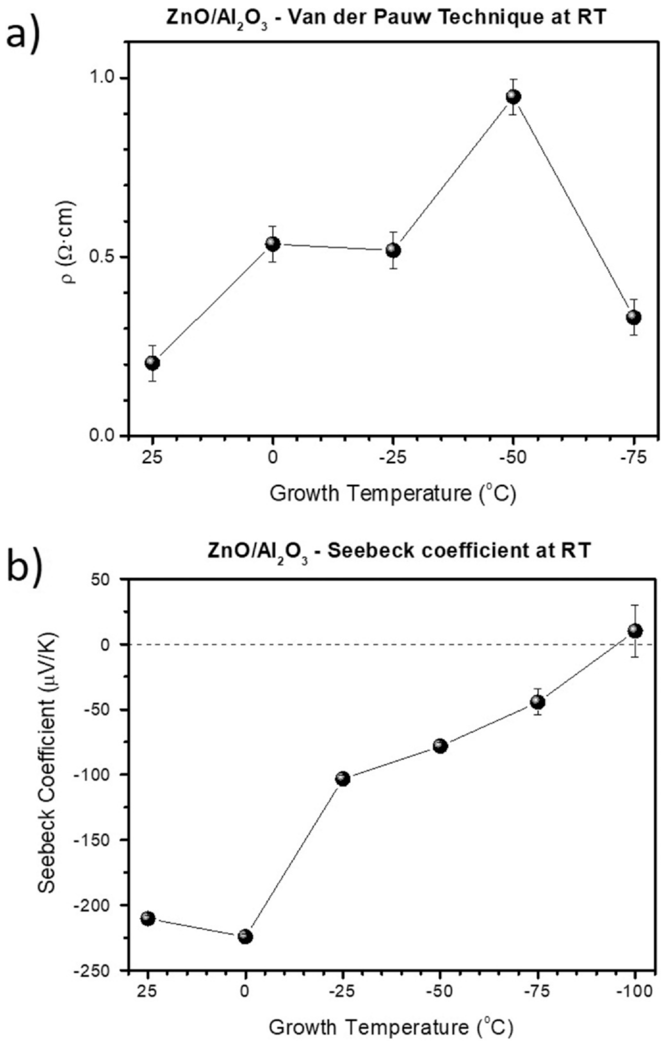

Fig. 9. a) Evolution of the electrical resistivity (ρ) with the growth temperature. b) Evolution of the Seebeck coefficient (S) with the growth temperature. The dashed line indicates the transition from n-type to p-type behaviour.

that depends on many interrelated factors, such as film structural ordering, roughness, porosity (or n-index), or nature of substrate/ film interface. Films grown at temperatures below RT present acceptable values of transmittance (> 80%), only decreasing (discarding RT as explained above) at very low temperatures (< −50 °C), precisely when the growth is more disordered, films present more defects, and the film/substrate interface develops its complex morphology and Zn-enrichment.

Electrical measurements performed at RT show significant variations as a function of the growth temperature of the films. On the one hand, Fig. 9a shows how the electrical resistivity (ρ) gradually increases around one order of magnitude, from 0.20 to 0.95 Ω·cm, between RT and − 50 °C samples. Subsequently, the electrical resistivity drops to 0.3 Ω·cm for − 75 °C. Samples grown at lower temperature could not be measured, possibly due to the presence of holes and breakings of the films (see Figs. 1, 2 and 3). These values are close to those reported for pure ZnO in the range $5{\cdot}10^{-3}$-100 Ω·cm [19,37,39,41,42], although by strictly controlling the Zn/O composition, higher resistivity values 10^{8}-10^{18} Ω.cm have been achieved [43]. Table 1 presents the electrical resistivity, transmittance and bandgap values of our ZnO films grown at RT and 0°C in comparison to other reports were none-doped ZnO films were deposited by different techniques at RT (higher temperatures are provided in case the particular reference varied this parameter). On the other hand, thermoelectric measurements of the Seebeck coefficient (S) in Fig. 9b show low values around − 225 μV/K for samples grown at higher temperatures, in agreement with other reports regarding semiconductor n-type ZnO films [44]. Nevertheless, as the growth temperature decreases, ZnO films show a sharp decrease of the S absolute value, even achieving low positive values for the − 100 °C sample (the experimental thermoelectric setup used here is not so sensitive to the continuity of the films as the four-probe methods). Although positive S values correspond to p-type doping, such small values are typically associated with a metallic character. For comparion, the values reported for metallic Zn are around 2.4 μV/K [45].

To understand this electrical behavior, the samples grown at 0 and − 75 °C have been measured at different temperatures (T). First, Fig. 10a shows the values of ρ as a function of T from 77 K (−196 °C) to 300 K (RT). The tendencies are just opposite: while sample grown at 0 °C shows a decrease of the resistivity with temperature, as expected for semiconductors, the sample grown at − 75 °C increases its resistivity, as expected for a metallic behavior. Second, Fig. 10b shows the Seebeck voltage (ΔV) as a function of the temperature difference along the sample (ΔT). As it can be seen, the sample grown at 0 °C presents a straight line, while that grown at − 75 °C shows a hysteresis-like cycle. This kind of curve shape has been proposed to be related to the time of response of different thermally activated charge-transport processes [46]. In this way, straight lines with negative slopes are associated with single n-type charge carriers (electrons) with unique response time. Together with the ρ vs T curve, this result confirms that samples grown at higher temperatures (RT, 0 °C) correspond to n-type ZnO semiconductors films. For lower growth temperatures, the hysteresis-like loop shown by the ΔV versus ΔT curve may indicate the presence of non-equilibrium states induced by fast variations of the temperature gradient (for example, processes involving excitation/trapping of charge carriers from shallow traps), or existence of multiple phases within the sample (in our case, metallic and oxidized zinc) [46].

Before discussing the origin of these optical and electrical results, we would like to highlight some considerations regarding the system's complexity. As shown before, ZnO films are not homogeneous, but more similar to a bilayer system for growths below 0 °C, where the columnar/interfacial system is gradually replaced by a polycrystalline/Zn-rich bilayer. This dual nature could have important consequences on the optical and electrical values, as the techniques used in this investigation give average information about the whole film. Besides, structural details regarding ZnO defects, such as the density of oxygen vacancies, the lattice strain, and the number of grain boundaries, may also play a significant role. Finally, the nature of the characterization techniques must also be taken into account. The absorbance value is an average of the whole film weighted by the relative thickness of the different layers. The same happens with the Seebeck data due to the thermal character of the measurements. Nevertheless, the van der Pauw approach is based on 2D conduction through a homogeneous film, and therefore bilayers systems could induce deviated results depending on the relative electrical resistivity and thickness.

Therefore, multiple factors must be considered to discuss the optical and electrical results. Such in-depth discussion is beyond the scope of the present article, and thus we will limit ourselves to a general overview taking into account the most critical features of ZnO films. In this sense, samples deposited at high temperature (RT and 0 °C) show an n-type semiconductor character with lower electrical resistivity than typical no-doped ZnO films. This improved conductivity could be related to a significant presence of oxygen vacancies, as shown by Raman spectroscopy. The development of these oxygen vacancies is energetically favorable if no oxygen-rich growth conditions are imposed [47] and would translate into high conductivities [43]. Yet, the origin of the natural n-type behaviour of

Table 1
Comparison of electrical resistivity, transmittance and bandgap values with those reported in the literature by different deposition techniques, such as e-beam evaporation, pulsed laser deposition (PLD), RF magnetron sputtering and filtered cathodic vacuum arc (FCVA).

Deposition technique	Substrate temperature (°C)	Resistivity (Ω·cm)	Transmittance (%)	Eg (eV)	Author, *(year)*[Ref]
e-beam	RT	$2 \cdot 10^{-1}$	60%	3.18	This article
	0 °C	$5 \cdot 10^{-1}$	> 80%	3.19	
e-beam	RT	$1.4 \cdot 10^{-1}$	Low	1.51	D. C. Agarwal et al. (2006) [37]
	400	$2.5 \cdot 10^{-2}$	High	3.26	
PLD	RT	–	–	3.31	B. L. Zhu et al. (2010) [38]
	350	–	–	3.27	
PLD	RT	$1.5 \cdot 10^{2}$-$4.6 \cdot 10^{5}$	85–95	3.34	S. Inguva, (2015) [39]
RF magnetron sputtering	RT	–	80–90	3.25	S. Youssef et al. (2008) [40]
	300	–	80		
	400	–	70		
RF magnetron sputtering	RT	$2 \cdot 10^{1}$-$4 \cdot 10^{2}$	–	–	Y. Wang et al., (2011) [41]
FCVA	RT	$4 \cdot 10^{-3}$-$5 \cdot 10^{-2}$	30–90	3.27–3.32	Y. G. Wang et al. (2003) [19]

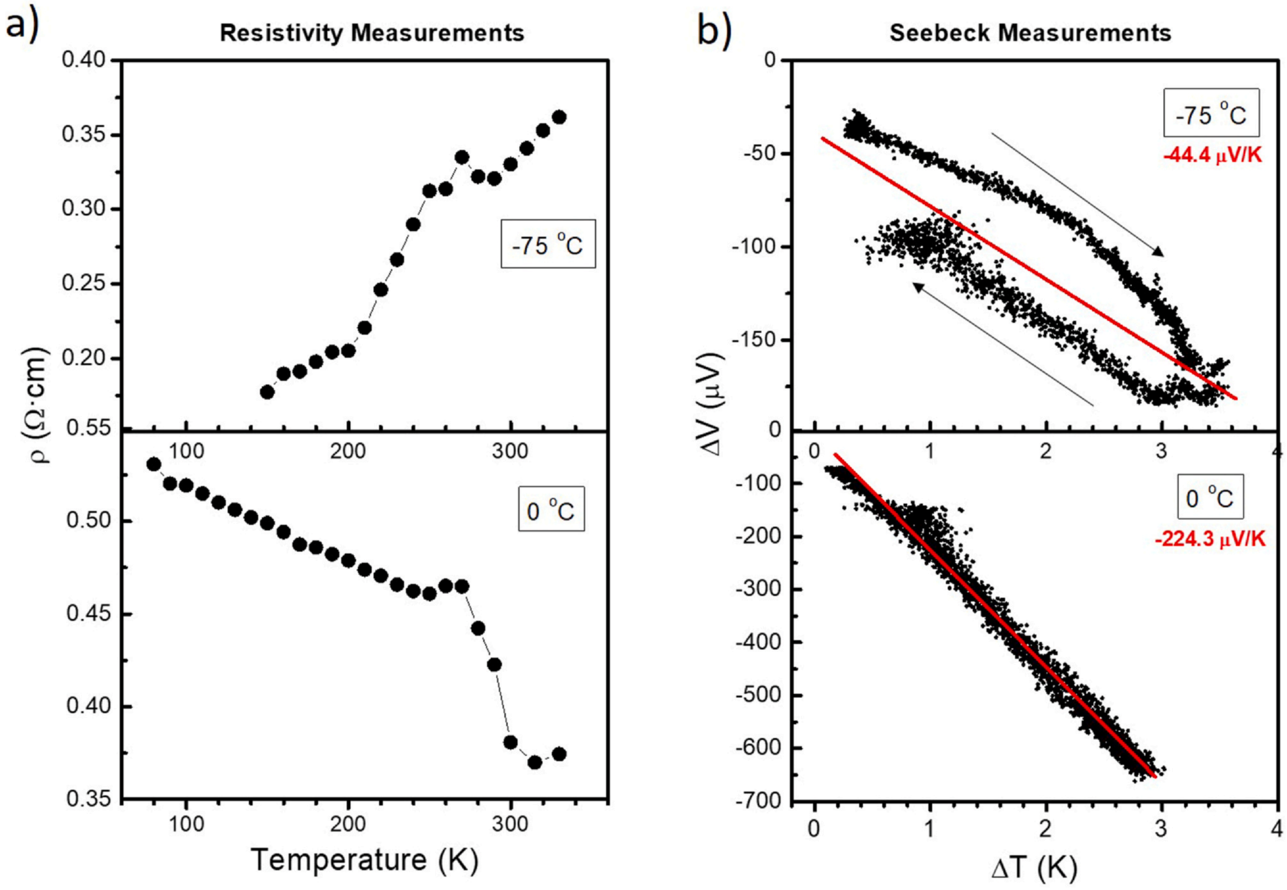

Fig. 10. a) Electrical resistivity measurements as a function of temperature for 0 °C (bottom) and − 75 °C (top) samples. b) Seebeck coefficient measurements as a function of the temperature difference along the sample for 0 °C (bottom) and − 75 °C (top) growths. The slope of the red lines corresponds to the Seebeck coefficient value.

non-doped ZnO is still controversial, and some authors attribute this to interstitial Zn [48] or natural hydrogen doping forming OH bonds with a length of 1 Å [49]. Moreover, as the growth temperature decreases (−50 °C) and films develop their bilayer nature, a loss of n-type character and an increase in electrical resistivity occurs. These facts coincide with an increased density of oxygen vacancies measured by Raman spectroscopy and larger average size of the crystallites. Although from the behavior of these two parameters a decrease of the electrical resistivity could be expected, it slightly increases. The reason could be explained by the oxygen vacancies, the bilayer nature, or both. In more detail, as a result of the absence of oxygen, the natural hydrogen doping could decrease due to fewer available OH bonds, leading to more resistive films with less n-type character. The electrical characterization is particularly remarkable for the − 75 °C sample, most probably owing to the Zn-rich interlayer. In this case, ΔV versus ΔT curve shows a hysteresis-like cycle that indicates the presence of multiple types of charge carriers, probably characterized by the participation of both metallic and oxide phases, at the same time that the ρ –T plot shows a metallic behavior. The reduction of the absolute Seebeck coefficient value could be related to the thermal nature of this measurement. The Zn-rich interfacial layer might induce a “short circuit”, becoming more critical as its thickness increases at lower temperatures. Finally, samples in the range from 0 to − 50 °C show acceptable values of optical transmittance, similar to those reported in the literature for RT films. Although many factors could determine the optical properties, the loss of transmittance at very low temperatures could be related to less ordered and more defective films, complex morphology of the film/substrate interface and Zn-enrichment.

4. Conclusions

ZnO thin films have been grown on Si and Al_2O_3 substrates at low temperatures (RT to −120°C). Subsequently, the films have been characterized in terms of structure and chemical composition, which have been correlated with their optical and electrical properties. First, we have found that such low temperatures have an important influence on the growth mode of the films and their morphology. As the temperature decreases, the surface diffusion of the evaporated atoms becomes more limited, which in turn leads to the formation of polycrystalline films and, sequentially, to a change in growth mode, i.e., from the van der Drift model found at higher temperatures to a bilayer growth mode in which the bilayer is composed of a less ordered interfacial layer and a second compact and columnar-based layer. The top columnar cover does not form at the lowest temperatures (< −100 °C) while a Zn-rich interface in contact with the substrate appears, possibly due to the lack of activation energy to overcome the intial barrier for ZnO nucleation at the substrate surface. For temperatures below − 100 °C, the formation of Zn-rich whiskers in contact with the substrate results in the rupture of the ZnO film and final loss of adhesion to the substrate. Besides, low temperatures can also affect the composition of the films, increasing the number of oxygen vacancies that might indirectly enhance the electrical conductivity compared to other pure ZnO growths performed under different conditions. However, at temperatures below − 50°C, together with the bilayer nature of the films, this could have a reverse effect by decreasing the available hydrogen forming OH bonds, and thus reducing the n-type character of less conductive films until the Zn-rich layer starts to dominate. Moreover, the growth temperature affects the transmittance without a significant variation of the band gap. From the electrical and optical measurements, it seems that the sample grown at a moderate low temperature of 0 °C shows the best compromise between good transparency levels and electrical conductivity values while preserving an explicit n-type conductivity. Particularly, the average transmittance is around 80%, much higher than our samples grown at RT and sharing similar values to other samples grown by other groups with this and others deposition techniques at RT or above. In order to understand more accurately the reason of the changes on the electrical and optical parameters, it would be advisable to perform an in-depth study on the type of defects developed during growth – for example, by photoluminescence – and to relate them to theoretical studies of defect formation under these extreme conditions, in which active thermal diffusion at the surface is limited.

CRediT authorship contribution statement

Carlos Morales: Conceptualization, Methodology, Investigation, Validation, Formal analysis, Writing - original draft, Data curation, Writing - review & editing. **Dietmar Leinen:** Investigation, Data curation, Formal analysis. **Adolfo del Campo:** Investigation, Data curation, Formal analysis. **José Ramón Ares:** Investigation, Data curation, Formal analysis. **Carlos Sánchez:** Writing - original draft, Resources. **Jan Ingo Flege:** Writing - original draft, Funding acquisition. **Alejandro Gutiérrez:** Writing - original draft, Resources. **Pilar Prieto:** Writing - original draft, Funding acquisition. **Leonardo Soriano:** Conceptualization, Methodology, Supervision, Resources, Funding acquisition, Writing - original draft, Writing - review & editing.

Declaration of Competing Interest

The authors declare that they have no known competing financial interests or personal relationships that could have appeared to influence the work reported in this paper.

Acknowledgments

This investigation has been funded by the Ministerio de Ciencia, Innovación y Universidades of Spain through the FIS2015-67367-C2-1-P project and by the Comunidad de Madrid through the NANOMAGCOST-CM P2018/NMT4321 project. One of the authors (C.M.) thanks Ministerio de Educación, Cultura y Deportes for FPU014/02020 grant. We also want to thank SEGAINVEX-UAM and SIdI-UAM for technical support.

Appendix A. Supporting information

Supplementary data associated with this article can be found in the online version at doi:10.1016/j.jallcom.2021.161056.

References

[1] Ü. Özgür, Ya.I. Alivov, C. Liu, A. Teke, M.A. Reshchikov, S. Doğán, V. Avrutin, S.-J. Cho, H. Morkoç, A comprehensive review of ZnO materials and devices, J. Appl. Phys. 98 (2005) 041301.
[2] B.M. Ataev, A.M. Bagamadova, A.M. Djabrailov, V.V. Mamedo, R.A. Rabadanov, Highly conductive and transparent Ga-doped epitaxial ZnO films on sapphire by CVD, Thin Solid Films 260 (1995) 19–20.
[3] H. Kim, C.M. Gilmore, J.S. Horwitz, A. Piqué, H. Murata, G.P. Kushto, R. Schlaf, Z.H. Kafafi, Transparent conducting aluminum-doped zinc oxide thin films for organic light-emitting devices, Appl. Phys. Lett. 76 (2000) 259–261.
[4] X.H. Zhou, Q.-H. Hu, Y. Fu, First-principles LDA+U studies of the In-doped ZnO transparent conductive oxide, J. Appl. Phys. 104 (2008) 063703.
[5] J. Rousset, E. Saucedo, D. Lincot, Extrinsic doping of electrodeposited zinc oxide films by chlorine for transparent conductive oxide applications, Chem. Mater. 21 (3) (2009) 534–540.
[6] D.-K. Hwang, M.-S. Oh, J.-H. Lim, S.-J. Park, ZnO thin films and light-emitting diodes, J. Phys. D. Appl. Phys. 40 (22) (2007) R387–R412.
[7] K.M. Sandeep, S. Bhat, S.M. Dharmaprakash, Structural, optical, and LED characteristics of ZnO and Al doped ZnO thin films, J. Phys. Chem. Solids 104 (2017) 36–44.
[8] L. Zhu, W. Zeng, Room-temperature gas sensing of ZnO-based gas sensor: a review, Sens. Actuat. A-Phys. 267 (2017) 242–261.
[9] K.-C. Lai, C.-C. Liu, C.-h Lu, C.-H. Yeh, M.-P. Houng, Characterization of ZnO:Ga transparent contact electrodes for microcrystalline silicon thin film solar cells, Sol. Energ. Mat. Sol. C 94 (3) (2010) 397–401.
[10] C. Klingshirn, ZnO: From basics towards applications, Phys. Stat. Sol. (b). 244 (2007) 3027–3073.
[11] Klaus Ellmer, Magnetron sputtering of transparent conductive zinc oxide: relation between the sputtering parameters and the electronic properties, J. Phys. D. Appl. Phys. 33 (4) (2000) R17–R32.
[12] R. Triboulet, J. Perrière, Epitaxial growth of ZnO films, Prog. Cryst. Growth Charact. Mater. 47 (2,3) (2003) 65–138.
[13] D.R. Sahu, S.-Y. Lin, J.-L. Huang, Improved properties of Al-doped ZnO film by electron beam evaporation technique, Microelectron. J. 38 (2) (2007) 245–250.
[14] T. Tynell, M. Karppine, Atomic layer deposition of ZnO: a review, Semicond. Sci. Technol. 29 (4) (2014) 043001.
[15] L. Znaidi, Sol–gel-deposited ZnO thin films: a review, MSEB 174 (2010) 18–30.
[16] W.I. Park, Controlled synthesis and properties of ZnO nanostructures grown by metalorganic chemical vapor deposition: a review, Met. Mater. Int. 14 (2008) 659–665.
[17] J.Y. Park, D.J. Lee, Y.S. Yun, J.H. Moon, B.-T. Lee, S.S. Kim, Temperature-induced morphological changes of ZnO grown by metalorganic chemical vapor deposition, J. Cryst. Growth 276 (2005) 158–164.
[18] S.-H. Cho, Effects of growth temperature on the properties of ZnO thin films grown by radio-frequency magnetron sputtering, Trans. Electr. Electron. Mater. 10 (6) (2009) 185–188.
[19] Y.G. Wang, S.P. Lau, H.W. Lee, S.F. Yu, B.K. Tay, Comprehensive study of ZnO films prepared by filtered cathodic vacuum arc at room temperature, J. Appl. Phys. 94 (2003) 1597–1604.
[20] W. Yang, Z. Liu, D.-L. Peng, F. Zhang, H. Huang, Y. Xie, Z. Wu, Room-temperature deposition of transparent conducting Al-doped ZnO films by RF magnetron sputtering method, Appl. Surf. Sci. 255 (2009) 5669–5673.
[21] M. Jalochowski, M. Hoffmann, E. Bauer, Pb layer-by-layer growth at very low temperatures, Phys. Rev. B 51 (1995) 7231–7238.
[22] J.F. Moulder, W.F. Stickle, P.E. Sobol, K.D. Bomben, J. Chastain (Ed.), Handbook of X-ray Photoelectron Spectroscopy, Perkin Elmer Corporation, Eden Prairie, Minnesota, USA, 1992.

[23] J.R. Ares, M. León, N.M. Arozamena, J. Sánchez-Páramo, P. Celis, I.J. Ferrer, C. Sánchez, Evolution of the Seebeck coefficient during the formation and crystallization of pyrite thin films, J. Phys. Condens. Matter 10 (1998) 4281–4289.

[24] A. van der Drift, Evolutionary selection, a principle governing grwoth orientation in vapor-deposited layers, Philips Res. Repts 22 (1967) 267–288.

[25] D.J. Lee, J.Y. Park, Y.S. Yun, Y.S. Hong, J.H. Moon, B.-T. Lee, S.S. Kim, Comparative studies on the growth behavior of ZnO nanorods by metalorganic chemical vapor deposition depending on the type of substrates, J. Cryst. Growth 276 (2005) 458–464.

[26] J.Y. Park, J.M. Lee, J.H. Je, S.S. Kim, Early stage growth behavior of ZnO nanoneedle arrays on Al_2O_3 (0001) by metalorganic chemical vapor deposition, J. Cryst. Growth 281 (2005) 446–451.

[27] S. Damyanova, L. Petrov, M.A. Centeno, P. Grange, Characterization of molybdenum hydrodesulfurization catalysts supported on ZrO_2-Al_2O_3 and ZrO_2-SiO_2 carriers, Appl. Catal. A-Gen. 224 (2002) 271–284.

[28] B.L. Henke, E.M. Gullikson, J.C. Davis, X-ray interactions: photoabsorption, scattering, transmission, and reflection at E=50–30000 eV, Z=1-92, At. Data Nucl. Data Tables 54 (2) (1993) 181–342.

[29] Christof Wöll, The chemistry and physics of zinc oxide surfaces, Prog. Surf. Sci. 82 (2007) 55–120.

[30] Yo Suna, E.N. Hoffman, P.-S. Lam, X. Li, Evaluation of local strain evolution from metallic whisker formation, Scr. Mater. 65 (5) (2011) 388–391.

[31] L. Huang, W. Jian, B. Lin, Y. Wen, L. Gu, J. Wang, Thermodynamic understanding of Sn whisker growth on the Cu surface in Cu(top)- Sn(bottom) bilayer system upon room temperature aging, J. Appl. Phys. 117 (2015) 215308.

[32] C. Morales, A. Black, F.J. Urbanos, D. Granados, J. Méndez, A. del Campo, F. Yubero, L. Soriano, Study of the interface of the early stages of growth under quasi-equilibrium conditions of ZnO on graphene/Cu and graphite, Adv. Mater. Interfaces 6 (2019) 1801689.

[33] No Benito, G. Recio, R. Escobar-Galindo, C. Palacio, Formation of antireflection Zn/ZnO core-shell nano-pyramidal arrays by O_2^+ ion bombardment of Zn surfaces, Nanoscale 9 (2017) 14201–14207.

[34] M. Scepanovic, M. Grujic-Brojcin, K. Vojisavljevic, S. Bernik, T. Sreckovicb, Raman study of structural disorder in ZnO nanopowders, J. Raman Spectrosc. 41 (2010) 914–921.

[35] J. Tauc, R. Grigorovici, A. Vancu, Optical properties and electronic structure of amorphous germanium, Phys. Status Solidi B 15 (1966) 627–637.

[36] J. Pankove, Optical Processes in Semiconductors, Dover Publications, New York, USA, 1971.

[37] D.C. Agarwal, R.S. Chauhan, Amit Kumar, D. Kabiraj, F. Singh, S.A. Khan, D.K. Avasthi, J.C. Pivin, M. Kumar, J. Ghatak, P.V. Satyam, Synthesis and characterization of ZnO thin film grown by electron beam evaporation, J. Appl. Phys. 99 (2006) 123105.

[38] B.L. Zhu, X.Z. Zhao, F.H. Su, G.H. Li, X.G. Wu, J. Wu, R. Wu, Low temperature annealing effects on the structure and optical properties of ZnO films grown by pulsed laser deposition, Vacuum 84 (2010) 1280–1286.

[39] S. Inguva, R.K. Vijayaraghavan, E. McGlynn, J.-P. Mosnier, Highly transparent and reproducible nanocrystalline ZnO and AZO thin films grown by room temperature pulsed-laser deposition on flexible Zeonor plastic substrates, Mater. Res. Express 2 (2015) 096401.

[40] S. Youssef, P. Combette, J. Podlecki, R. Al Asmar, A. Foucaran, Structural and optical characterization of ZnO thin films deposited by reactive rf magnetron sputtering, Cryst. Growth Des. 9 (2) (2009) 1088–1094.

[41] Y. Wang, Z.J. Peng, Q. Wang, X.L. Fu, Tunable electrical resistivity of oxygen-deficient zinc oxide thin films, Surf. Eng. 33 (3) (2011) 217–225.

[42] G. Heiland, E. Mollwo, F. Stöckmann, Electronic processes in Zinc Oxide, Solid State Phys. 8 (1959) 191–323.

[43] D.L. Raimondi, E. Kay, High resistivity transparent ZnO thin films, J. Vac. Sci. Technol. A 7 (1970) 96–99.

[44] X. Qu, W. Wang, S. Lv, D. Jia, Thermoelectric properties and electronic structure of Al-doped ZnO, Solid State Commun. 151 (2011) 332–336.

[45] D.M. Rowe, CRC Hanbook of thermoelectric materials, CRC Press, Boca Raton, New York, USA, 1995.

[46] I.J. Ferrer, P. Díaz-Chao, A. Pascual, C. Sánchez, Hysteresis-like behaviour of the thermoelectric voltage in photovoltaic materials, Thin Solid Films 511–512 (2006) 177–181.

[47] A.F. Kohan, G. Ceder, D. Morgan, C.G. Van de Walle, First-principles study of native point defects in ZnO, Phys. Rev. B 61 (2000) 15019–15027.

[48] D.C. Look, J.W. Hemsky, J.R. Sizelove, Residual Native Shallow Donor in ZnO, Phys. Rev. Lett. 82 (1999) 2552–2555.

[49] C.G. Van de Walle, Defect analysis and engineering in ZnO, Phys. B 899 (2001) 308–310.